

## Impact of temporal compositing on nighttime light data and its applications

Qiming Zheng <sup>a,\*</sup>, Qihao Weng <sup>b</sup>, Yuyu Zhou <sup>c</sup>, Baiyu Dong <sup>d</sup>

<sup>a</sup> Centre for Nature-based Climate Solutions, and Department of Biological Sciences, National University of Singapore, 14 Science Drive 4, Singapore 117543, Singapore

<sup>b</sup> Department of Land Surveying and Geo-Informatics, Hong Kong Polytechnic University, Hung Hom, Kowloon, Hong Kong

<sup>c</sup> Department of Geological and Atmospheric Sciences, Iowa State University, Ames 50011, USA

<sup>d</sup> Institute of Applied Remote Sensing and Information Technology, College of Environmental and Resource Sciences, Zhejiang University, Hangzhou, Zhejiang 310058, China

### ARTICLE INFO

#### Keywords:

Nighttime light imagery  
Daily VIIRS images  
Temporal compositing  
Geographic variation  
NTL applications  
Urbanization

### ABSTRACT

In recent decades, nighttime light (NTL) images have been widely explored to portray human footprints. Most of the studies used monthly or yearly temporal composite NTL products as a solution for invalid observations due to cloud coverage and outlier signals. However, the impact of temporal compositing on NTL data and its applications remains largely unclear. Here, we utilized over 180,000 daily NTL tiles from NASA's Black Marble VIIRS product (VNP46A2, 2012–2020), covering 230 cities from China and the United States, to delve into the influence of temporal compositing on valid pixel coverage and spatiotemporal pattern of NTL data and the performance of three representative types of NTL-based applications. Our analysis showed temporal compositing was an imperative and efficient solution to the prevailing invalid observations. On average a 16-day composite was required to ensure at least 95% of valid pixel coverage for a city, where a longer composite period was needed for cities in a pluvial temperate climate zone. Compositing daily NTL data into a 3-day to 31-day period markedly reduced its spatiotemporal variation and incurred a 3–9 nWatts/cm<sup>2</sup>/sr, or 22%–37%, absolute difference in NTL magnitude, which was particularly high in developed cities and intra-city areas. We attributed such effect to the number of valid observations available for generating the composite data and the extremely high variation in daily NTL stemmed from human activities, as well as the uncertainties in VNP46 product and VIIRS instrument. The impact of temporal compositing on NTL-based applications varied greatly, from insignificant to very sensitive, across application types and spaces. Our analysis provides a comprehensive understanding of the capability and uncertainties in NTL data processing and applications, facilitating end-users to make the best use of NTL observations in high temporal frequency.

### 1. Introduction

Nighttime light (NTL) from space offers a novel point-of-view in portraying the extent and intensity of human footprints (Elvidge et al., 1997; Levin et al., 2020). Since the 1970s, a succession of satellite sensors have been developed and utilized to detect NTL at both global and regional scales, including Defense Meteorological Satellite Program-Operational Linescan System (DMSP-OLS) (Croft, 1978; Imhoff et al., 1997), Visible Infrared Imaging Radiometer Suite (VIIRS) of Suomi-NPP satellite (Román et al., 2018), Luojia-01 (Li et al., 2018), Jilin1-03B (Guk and Levin, 2020; Zheng et al., 2018), as well as images taken from the International Space Station (Sánchez de Miguel et al., 2021). In recent decades, there is an extensive surge in using NTL data as a proxy

of human activities, such as mapping urban growth (Elvidge et al., 1997; Sutton, 2003; Zhou et al., 2018), estimating socioeconomic variables (e.g., population and GDP) (Anderson et al., 2010), evaluating the risks to natural disasters (Román et al., 2019), and assessing the impact of artificial light encroachment on natural ecosystems (Sanders et al., 2020).

Nevertheless, NTL data has its downside—coverage of valid observation is heavily constrained by issues including cloud cover, lunar irradiance, and stray light (Miller and Turner, 2009). In addition, NTL data is also affected by many environmental factors and their geographic variation, such as seasonality (Levin, 2017) and atmospheric scattering (Elvidge et al., 2017). To address these issues, most of the current end-users based their research on temporal composite NTL products

\* Corresponding author.

E-mail addresses: [qmzheng@nus.edu.sg](mailto:qmzheng@nus.edu.sg), [qmzheng@zju.edu.cn](mailto:qmzheng@zju.edu.cn) (Q. Zheng), [qihao.weng@polyu.edu.hk](mailto:qihao.weng@polyu.edu.hk) (Q. Weng), [yuyuzhou@iastate.edu](mailto:yuyuzhou@iastate.edu) (Y. Zhou), [11914074@zju.edu.cn](mailto:11914074@zju.edu.cn) (B. Dong).

aggregated from cloud-free and high-quality daily observations within a certain composite period (also called composite scale or composite interval), such as yearly composite DMSP-OLS and monthly/yearly composite VIIRS (Imhoff et al., 1997; Levin et al., 2020). Composite data producers have been making substantial efforts in controlling the noise level in the composite process and generating high-quality data (Elvidge et al., 2021).

However, the rapid urbanization poses an urgent demand for high frequency observations, e.g., in shorter composite periods than monthly and yearly, to provide a more temporally explicit and timely change characterization (Zhu et al., 2019). To fulfill such demand, the following key questions regarding the impact of temporal compositing on NTL data should be answered:

- **Coverage of valid observations:** whether high-quality NTL coverage is attainable at a high temporal frequency (e.g., daily or sub-monthly) via temporal compositing;
- **Fidelity of spatiotemporal pattern:** whether/how different composite periods influence the spatiotemporal pattern of NTL;
- **Performance of NTL-based applications:** how the performance of NTL-based applications vary across composite periods;
- **Geographic variability:** How the abovementioned issues vary over space.

These knowledge gaps mainly result from difficulties in accessing to preprocessed high-quality daily NTL images used for generating the composite product. Albeit with a few NTL datasets available at daily scale, such as Jilin1-03B, EORS-B, Luojia-01, and image from International Space Station, they are not suitable for a robust investigation of the above-mentioned issues due to their limited spatial and temporal data coverage (Li et al., 2018; Sánchez de Miguel et al., 2019). Recently, a series of high-quality daily VIIRS products have been released and made freely accessible to the public, such as the NASA's Black Marble nighttime lights product suite (VNP46) (Román et al., 2018), NOAA-20 VIIRS (Hong et al., 2021), and the new VIIRS product from Earth Observation Group (EOG) at Payne Institute (Elvidge et al., 2020).

In this study, we aimed at leveraging a huge volume of VNP46 images to carry out a robust and in-depth investigation into how temporal compositing affects (1) valid pixel coverage; (2) the spatiotemporal

pattern of NTL time series; and (3) the performance of representative types of NTL-based applications.

## 2. Study area and datasets

In this research, 230 cities were selected as study area, including 114 prefectural cities and 116 cities from China and the United States, respectively (Fig. 1). These major urbanized areas are hotspots and ideal test-bases of NTL studies (Liu et al., 2012; Xie et al., 2019). Our test cities cover a wide variety of background conditions in terms of socioeconomic status (e.g., population, 4 thousand to 34 million), geolocations ( $18^{\circ}\text{N}$  to  $48^{\circ}\text{N}$ ), landscape configurations (e.g., polycentric and monocentric), and environment and climate conditions (e.g., tropical and alpine). Such diversified city selection and the consequent huge number of input data with over 27 million NTL pixel time series ensured the robustness of our analysis (Reba and Seto, 2020). For a clear and concise demonstration, we mainly showcase our results with cities of China, while results derived from cities of the United States are presented in Supplementary Data.

Our analysis was based on the moonlight and atmosphere corrected NTL of NASA's VIIRS Black Marble product (VNP46A2, Collection V001) (Román et al., 2018). VNP46A2 contains seven layers, offering daily images of NTL radiance and the corresponding quality control information at a 15 arc-second spatial resolution (Table 1) (NASA, 2018). VNP46A2 is a further refinement of VNP46A1 at-sensor TOA NTL product. Compared to the commonly-used monthly composite VIIRS data, the superiority of VNP46 lies in its temporal resolution and more importantly, in its overall data quality. The quality of VNP46A2 is guaranteed by a series of routine corrections, including lunar BRDF, cloud, terrain, atmospheric, airglow, stray light, as well as a substantial sensitivity enhancement of low-lit structures (Wang et al., 2021a). It enables us to minimize the biases caused by extraneous artifacts (e.g., lunar irradiance) to our subsequent analysis. We downloaded all VNP46A2 tiles overlapping with the 230 test cities between January 19, 2012 and December 31, 2020 from NASA's Level 1 and Atmosphere Archive and Distribution System Distributed Active Archive Center (LAADS-DAAC; <http://ladsweb.modaps.eosdis.nasa.gov>, last access: May 1, 2021). In total, over 180,000 VNP46A2 tiles and 27 million pixels with approximately 2900 daily observations for each pixel were

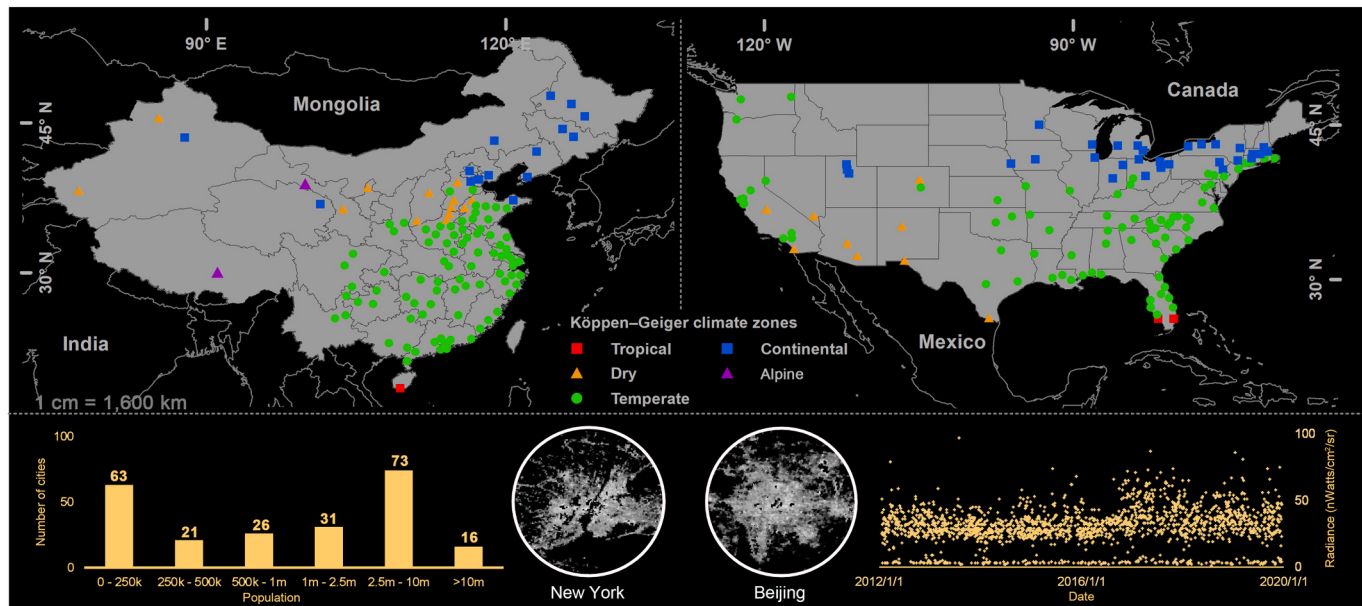


**Fig. 1.** Selected cities, from China ( $N = 114$ ) and the United States ( $N = 116$ ), with their corresponding Köppen–Geiger climate zones. The bottom-left histogram summarizes the population of selected cities. The scatter plot at the bottom-right shows the NTL time series of a typical urban pixel of Beijing, China, derived from the BRDF-corrected of VNP46A2 VIIRS product.

**Table 1**  
Layer information of VNP46A2 product.

Label	Layer	Unit	Description
L1*	BRDF-corrected NTL	nWatts·cm <sup>-2</sup> ·sr <sup>-1</sup>	Daily NTL
L2	Lunar irradiance	nWatts·cm <sup>-2</sup> ·sr <sup>-1</sup>	
L3	Gap-filled BRDF-corrected NTL	nWatts·cm <sup>-2</sup> ·sr <sup>-1</sup>	Outliers/no-retrievals are gap-filled
L4	Latest high-quality retrieval	Number of days	
L5*	Mandatory quality flag	Unitless	Retrieval quality High quality: L5 = 0 or 1 Outliers/no-retrieval: L5 = 2/255
L6*	Quality flag of cloud mask	Unitless	Detailed information about mask quality of cloud/shadow/snow
L7*	Snow flag	Unitless	Indication of snow/ice

Note: Please refer to the V1.2 Algorithm Theoretical Basis Document (ATBD) of Black Marble product for further details (Wang et al., 2021b). \*: layers used in this study.

used to buttress our analysis.

The administrative boundary and population data of test cities of China and the United States were obtained from the Geographical Information Monitoring Cloud Platform (<http://www.dsac.cn/>) and statistical yearbook of China, and the United States Census Bureau (<https://www.census.gov/>), respectively. The floor number of each building footprint of Shanghai, China, as an alternative proxy of building height, was obtained from Amap (<https://amap.com/>). MODIS MCD12Q1 land cover product (Sulla-Menashe et al., 2019), MODIS MOD13A1 16-Day NDVI product (Didan, 2015), and Monthly Global Precipitation Measurement (Huffman et al., 2015) were pre-processed and exported via Google Earth Engine (Gorelick et al., 2017). Köppen–Geiger climate classification scheme was employed to present climate conditions of test cities (<http://koeppen-geiger.vu-wien.ac.at/>).

### 3. Methods

#### 3.1. Data preprocessing

The BRDF-corrected daily NTL radiance layer (L1) served as the main input for analysis, whilst mandatory quality flag (L5), quality flag of

cloud mask (L6) and snow flag (L7) were acquired to complement supporting quality control information (Table 1). It should be noted that all the analysis started from pixel-level (pixel time series) and the pixel-level results were then summarized to city-level mean (individual examples can be found in Supplementary Data).

We aimed at generating daily VIIRS pixel with NTL radiance under seven composite periods from 1-day (daily) to 31-day. The composite period refers to the temporal window (i.e., how many daily observations) that is considered to create the composite data (Hu and Brunsell, 2013; Hüttich et al., 2011). For each pixel time series, we adopted a moving window algorithm and moved the window forward day by day to calculate the average radiance under seven window sizes spanning 1-, 3-, 5-, 7-, 9-, 15-, 31-day (Fig. 2) (Hu and Brunsell, 2013). Only high-quality retrievals (i.e., valid observation, L5 = 0 or 1) were used for creating the composite data, while low-quality retrievals (i.e., invalid observation, L5 = 2 or 255) were excluded. The pixels with radiances less than 0.5 nWatts/cm<sup>2</sup>/sr were masked out to eliminate the residual background noises (Wang et al., 2021b).

#### 3.2. Temporal compositing influence on valid pixel coverage

In addition to low-quality retrievals (L5 = 2 or 255; Table 1), we found some certain year-DOY combinations had no downloadable tile in LAADS-DAAC, called missing tile issue in this study. Averaging over all the pixel time series for 230 test cities from 2012 to 2020, about 64% of daily observations, equal to 233 days per year, were subject to either low-quality retrievals or missing tile issue. As such, it was barely possible to cover the entire study area (e.g., city) with valid pixels by a single daily VIIRS image. Here, to explore how valid pixel coverage varied across composite period, we calculated the mean percentage of valid pixel coverage of each city in each DOY (day of the year, DOY ∈ [1,365]). For each city, we repeated this calculation to obtain the valid coverage-DOY-period relationship under all seven composite periods. Besides, we leveraged the quality flag layers to trace the cause of invalid observations by cloud coverage, snow coverage and missing tile issue.

Based on the resulting valid coverage-DOY-period relationship, we developed a new index—Period<sub>valid\_cvg (α)</sub>—to describe the minimum composite period that can suffice more than α% of valid pixel coverage for a certain city. Period<sub>valid\_cvg (α)</sub> demonstrated the capability of NTL data in presenting details in high temporal frequency. To calculate Period<sub>valid\_cvg (α)</sub> of each test city, we first analyzed Period<sub>valid\_cvg (α)</sub> at

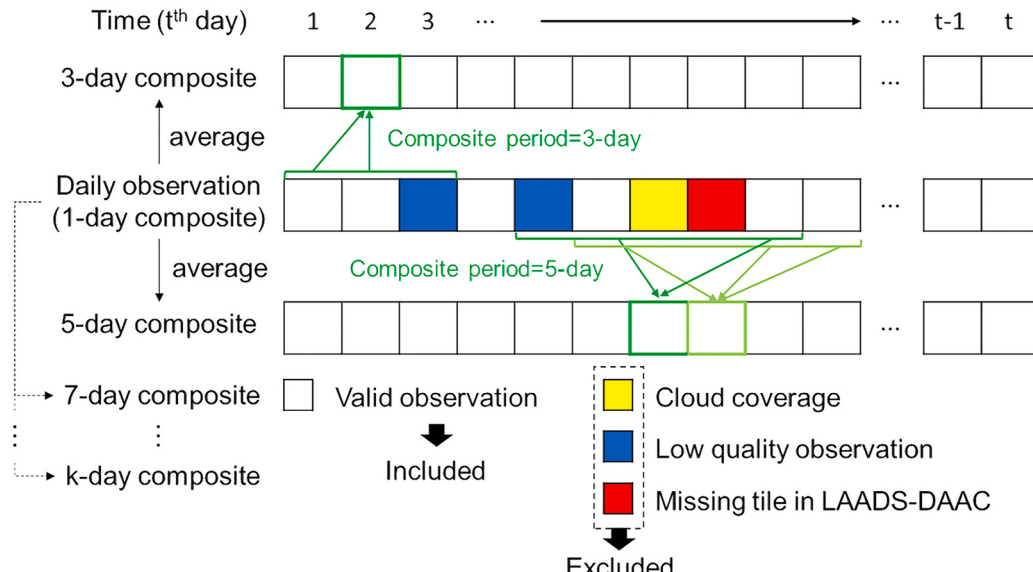


**Fig. 2.** Illustrative diagram of creating composite NTL data.

each DOY, presented by a  $\text{Period}_{\text{valid\_cvg}}(\alpha)$ -DOY curve. Then,  $\text{Period}_{\text{valid\_cvg}}(\alpha)$  of the city was determined by the mean  $\text{Period}_{\text{valid\_cvg}}(\alpha)$  across all DOYs. We set  $\alpha = 95$  for our analysis, while results from other  $\alpha$  values were presented in Fig. S1. A longer  $\text{Period}_{\text{valid\_cvg}}(\alpha)$  indicates that a city is more vulnerable to the influence of cloud and snow coverage and is harder to obtain sufficient valid pixel coverage. We also explored the spatial variation of  $\text{Period}_{\text{valid\_cvg}}(\alpha)$  and its relationship to latitude, climate zone, and precipitation conditions.

### 3.3. Temporal compositing influence on the spatiotemporal pattern

The spatiotemporal variation of NTL is the basis of NTL data processing, modelling and applications. Here, we shed light on the impact of temporal compositing on the spatiotemporal pattern of NTL data. Instead of using NTL time series under each composite period directly, we based the analysis on the modelled NTL from a time series model. The rationale was that the real NTL pattern was prone to be veiled by enormous data variation and outlier signals (Elvidge et al., 2020). Fitting a time series model is an effective way to isolate noise and outliers (Zhu, 2017) and reduce the impact of the widespread low-quality observations in daily observations. We fitted the NTL time series of each pixel with a Logistic-Harmonic model (LogH model; Eq. 1). The LogH model divides the NTL time series into the combination of trend component and seasonality component (Zheng et al., 2021).

$$\text{NTL}_{ts}(t) = \frac{a}{1 + e^{bt+c}} + d + \sum_k^2 \left[ f_k \sin\left(\frac{2\pi k \cdot t}{T}\right) + g_k \cos\left(\frac{2\pi k t}{T}\right) \right] + \epsilon \quad (1)$$

Where  $\text{NTL}_{ts}$  is a function of time  $t$  ( $t$ -th observation of the pixel time series), presenting the daily NTL radiance described by a logistic term (trend) and 2 harmonic terms (seasonality). It comprises the following parameters: magnitude of change ( $a$ ), change rate ( $b$ ), timing of change ( $c$ ), pre-change or post-change radiance value ( $d$ ), and amplitude factor of seasonal effect ( $f_k$  and  $g_k$ );  $e$  is the base of the natural logarithm, while  $T = 365$  is the period of harmonic terms.

We compared the difference between modelled NTL derived from k-day composite data and those from daily observation (1-day composite). This analysis allows us to ascertain how much NTL difference was caused due to temporal compositing and how the difference varied inter- and intra-annually. To further explore the underlying mechanism of the effect, we counted the number of valid observations within each period and calculated the standard deviation of NTL magnitude over space (all pixels in a city) and time (all observations of a pixel) for each city (Hu and Brunsell, 2013). We also regressed NTL difference with the GDP of the test cities and building height of each pixel of Shanghai to reveal the influence from socioeconomic conditions and urban vertical structure, respectively. In addition, to avoid the impact of model selection on the results, the same analysis was applied to another commonly-used time series model—the Breaks for Additive Season and Trend (BFAST) as a reassurance approach (Verbesselt et al., 2010).

### 3.4. Temporal compositing influence on NTL-based applications

The impact of composite period on the spatiotemporal pattern of NTL would propagate to and affect the performance of NTL-based applications. Since NTL-based applications rely on different spectral and/or temporal characteristics of NTL data (Zhao et al., 2018), we postulated different types of applications would have varied responses to composite period. Three representative and distinct types of NTL-based applications were selected, including characterizing gradual changes, detecting abrupt changes and monitoring re-occurring seasonal changes (Table 2). The selection rationale lied in two aspects. First, a traditional application was chosen since applications, like spectral feature-based urban mapping, are still the mainstream of current NTL studies. Second, we put more weight on the applications relying on high frequency observations (e.g., daily and sub-monthly), such as breakpoint timing detection and

**Table 2**  
Three key types of representative NTL-applications.

Application types	Applications	Methods (type & reference)	Performance indicators	Similar applications
Characterizing gradual changes	Spectral-based urban growth mapping	Thresholding method (Liu et al., 2012)	Overall accuracy (%)	Henderson et al. (2003); Xiao et al. (2014)
	Spectral + temporal-based urban growth mapping	Machine Learning (Zheng et al., 2021)	Overall accuracy (%)	Xie et al. (2019); Zhou et al. (2014)
Detecting abrupt changes	Breakpoint timing detection	Time series modelling + change detection (Verbesselt et al., 2010)	Timing of the detected breakpoint in NTL time series	Small and Souza (2021); Zheng et al. (2019)
Monitoring seasonal changes	Seasonality modelling	Time series modelling (Xie et al., 2019)	$R^2$	Roman and Stokes (2015); Zhao et al. (2020)

urban mapping based on spatial and temporal features. These applications reflected major dimensions of NTL studies enabled by newly-released daily NTL data. Analyzing the temporal compositing's impact on these applications helped to build a clear picture of the advances and potential uncertainties of high frequency NTL data.

Here, we briefly described each selected application, while methodological details can be found in the provided reference (Table 2):

#### • Characterizing gradual changes

- Urban growth mapping based on spectral features: using NTL radiance at a certain time (spectral feature) and an optimal thresholding method to map urban areas (Liu et al., 2012), which was one of the most commonly used traditional approaches in NTL-based urban mapping.
- Urban growth mapping based on spectral and temporal features: using spectral and temporal features (e.g., trajectory shape) extracted from NTL time series and a Random Forest classifier to map urban areas (Zheng et al., 2021). Incorporating temporal features has received a lot of attention in recent NTL-based urban mapping, which would be further advanced with high frequency NTL data (Tang et al., 2021).

#### • Detecting abrupt changes

The capability of detecting abrupt short-term changes in NTL time series will be greatly improved with the help of high frequency observations. This capability is useful for applications such as detecting power outage/recovery (Roman et al., 2019) and analyzing the effects of the COVID-19 lockdown on outdoor illumination (Bustamante-Calabria et al., 2021). We employed the breakpoint detection method of Verbesselt et al. (2010) to identify the timing of abrupt changes in NTL time series.

#### • Monitoring re-occurring seasonal changes

Another advantage enabled by high frequency NTL observations is monitoring re-occurring seasonal changes in human activities, e.g., holidays (Roman and Stokes, 2015) and human migration (Chen, 2020). We fitted each pixel time series with a seasonality model proposed by Xie et al. (2019) to assess the capability of NTL data in monitoring seasonal changes across different composite periods (Eq. 2):

$$NTL_{intra}(DOY) = NTL_{intercept} + \sum_k^2 \left[ a_k \sin\left(\frac{2\pi k \cdot DOY}{T}\right) + b_k \cos\left(\frac{2\pi k \cdot DOY}{T}\right) \right] + \epsilon \quad (2)$$

Where  $NTL_{intra}$  is a function of  $DOY \in [1, 365]$ , explaining the intra-annual variation of daily NTL radiance;  $NTL_{intercept}$  presents the intercept;  $T$  refers to the period of observation, which is set to 365;  $a_k$  and  $b_k$  present the amplitude factors of seasonality. The number of harmonic term  $k$  is set as 2 to account for the annual and semi-annual seasonal periods.

#### • Analysis

To assess the impact of temporal compositing on the performance of each selected application, we tested each application with input data in different composite periods, from daily observation to k-day composite, and compared the resulting performance indicators (Table 2). The coefficient of variation (CV) was also calculated to examine how such effect varied across application types and space.

## 4. Results and discussion

### 4.1. Temporal compositing influence on valid pixel coverage

The mean valid pixel coverage (%) of all test cities of China showed a noticeable improvement as the composite period increased from 1-day to 31-day (Fig. 3a). Lacking valid pixels was a severe issue in short composite periods ( $\leq 5$ -day). It led to massive data gaps in study area, where on average only  $59 \pm 7\%$  of pixels in a city could sustain consistent and valid coverage. As the composite period exceeded 9-day, the percentage of valid coverage increased to  $90 \pm 19\%$ . The mean  $Period_{valid\_cvg(95)}$ -DOY curve revealed that in almost all DOYs it was impossible to secure sufficient valid coverage without temporal compositing, consequently translating to a mean  $Period_{valid\_cvg(95)}$  of  $16 \pm 7$  days (Fig. 3b). In other words, on average a  $16 \pm 7$  days composite period was needed to ensure at least 95% of valid pixel coverage at any DOY for a city (see different  $Period_{valid\_cvg(95)}$  in Fig. S1). Nevertheless, we found that  $Period_{valid\_cvg(95)}$  of all test cities of China ( $N = 114$ ), as well as the US ( $N = 116$ ), were below 31 days. These findings indicate temporal compositing is an imperative and effective solution to achieve

sufficient valid pixel coverage city-wide. More importantly, our findings prove that it is achievable for NTL data to obtain high temporal frequency details (e.g., every  $16 \pm 7$  days), instead of at a yearly or monthly period.

The spatial distribution of  $Period_{valid\_cvg(95)}$  showed that it was negatively associated with latitude ( $R^2 = 0.53$ ; Figs. 4a & 4b). Cities in low latitude required a longer  $Period_{valid\_cvg(95)}$  to maintain sufficient valid coverage, e.g., Guangzhou (23-day) and Chongqing (28-day), while  $Period_{valid\_cvg(95)}$  of cities in middle latitude ( $> 35^\circ$ ) was prominently shorter, such as Beijing (7-day) and Dalian (9-day). A closer comparison of the  $Period_{valid\_cvg(95)}$ -DOY curves of cities among temperate, dry and continental climate zones revealed the intra-annual pattern of  $Period_{valid\_cvg(95)}$  varied across local climate conditions (Figs. 4g-4i). For cities in dry and continental regions which are mainly distributed in medium and high latitude areas,  $Period_{valid\_cvg(95)}$  was relatively longer during the summer (DOY = 150–240) and part of the winter (DOY = 1–20) than in other DOYs. By comparison,  $Period_{valid\_cvg(95)}$  of cities in temperate climate zones stayed long for almost the entire year (Fig. 4g). The Wilcoxon Signed-Rank test indicates that  $Period_{valid\_cvg(95)}$  of cities in temperate regions (18-day) are significantly longer than that of cities in dry (11-day;  $P < 0.01$ ) and continental (10-day;  $P < 0.01$ ) regions. However, no statistical difference was found between the  $Period_{valid\_cvg(95)}$  of cities in dry and continental regions. This discrepancy is attributable to differences in regional cloud coverage and precipitation pattern. Summarizing the corresponding quality control layers, it was found that the invalid pixels were mainly incurred by cloud coverage (89%) and, to a lesser extent, the snow coverage (22% for dry and continental regions only), while less than 2% of the invalid pixels were caused by missing tile issue (Figs. 4d-4e). Besides, the  $Period_{valid\_cvg(95)}$  was positively related to annual precipitation ( $R^2 = 0.43$ ,  $P < 0.01$ ; Fig. 4c). Due to the year-round abundant rainfall in temperate regions, the valid pixel coverage of cities therein is heavily limited by cloud, consequently leading to a long  $Period_{valid\_cvg(95)}$  throughout the year. The rainfall of dry and continental regions in China is mostly brought by the summer monsoon, therefore only resulting in a long  $Period_{valid\_cvg(95)}$  in the summer (Gemmer et al., 2004). Besides, the nonlinearity in the relationship between  $Period_{valid\_cvg(95)}$  and latitude/precipitation suggests these factors are not mutually exclusive and may

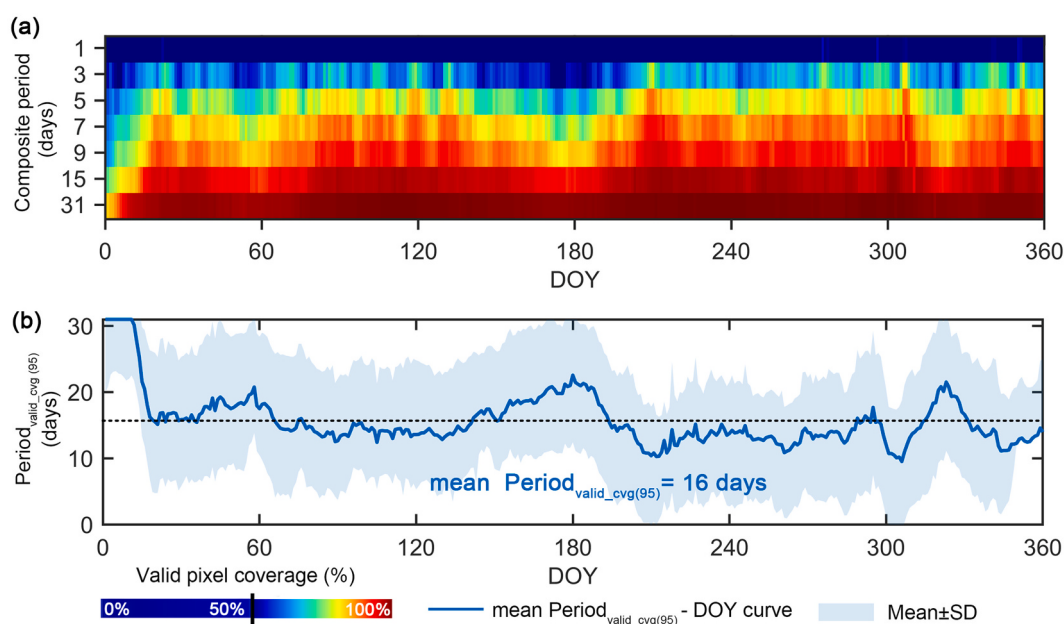


**Fig. 3.** Mean valid pixel coverage (%) across seven composite periods (a) ( $N = 114$  test cities of China). Mean (blue plot) and standard deviation (SD; shaded area) of the  $Period_{valid\_cvg(95)}$ -DOY curve (b). For a better demonstration, only  $DOY \in [1, 360]$  is presented. (For interpretation of the references to colour in this figure legend, the reader is referred to the web version of this article.)

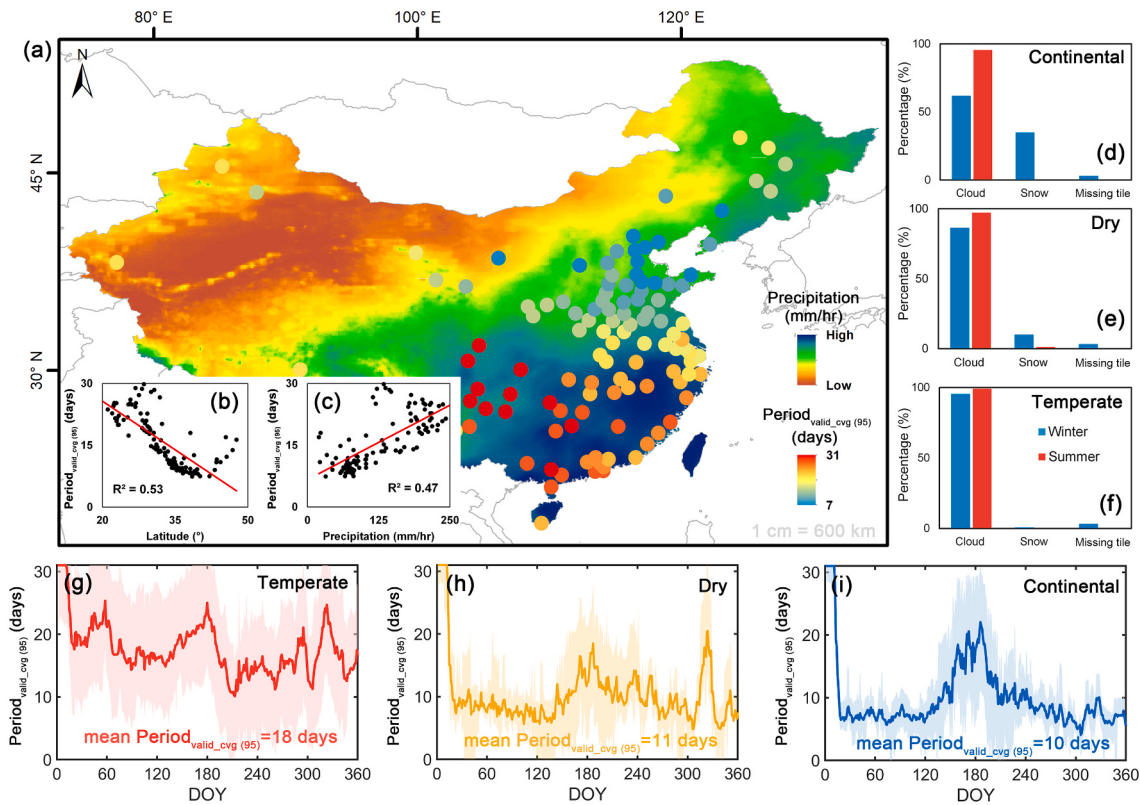


**Fig. 4.** Spatial pattern of the Period<sub>valid\_cvg</sub> (95) of each city (dot; a). The relationship between Period<sub>valid\_cvg</sub> (95) and the latitude (b) and annual mean precipitation (c). Causes of invalid observation (%) for cities in temperate (d), dry (e) and continental (f) regions. Mean and standard deviation (shaded areas) of the Period<sub>valid\_cvg</sub> (95)-DOY curve of cities in temperate (g), dry (h) and continental (i) regions.

even have an interactive effect. In addition, the long Period<sub>valid\_cvg</sub> (95) can also be induced by the solar angle cut-off issue which occurs frequently during the summer. The observations with a solar zenith angle lower than 108° will be assigned as no-data and replaced by fill value in the processing chain of the Black Marble product (Wang et al., 2021b).

#### 4.2. Temporal compositing influence on the spatiotemporal pattern of NTL

To illustrate the impact of temporal compositing on the spatiotemporal pattern of NTL, we compared the difference in the modelled NTL magnitude (NTL<sub>t</sub>) between composite data and daily observation. Fig. 6 shows the mean statistics aggregated from all test cities of China. At the first glance, we found the temporal compositing resulted in a noticeable

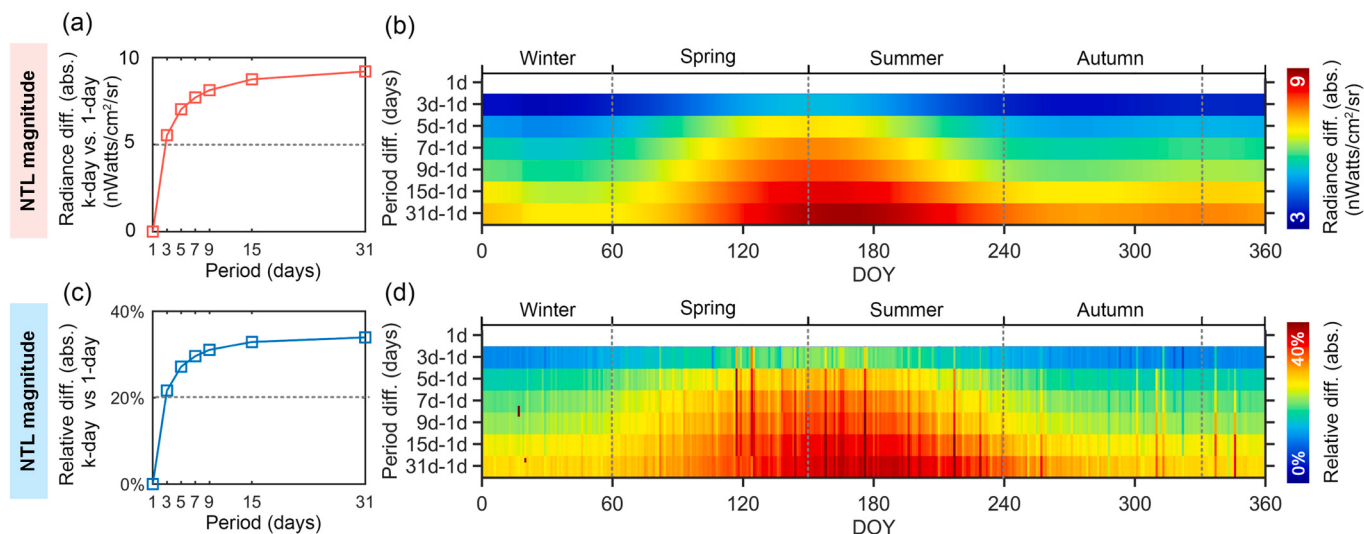


**Fig. 5.** Impact of temporal composite period on the modelled NTL magnitude. The upper and lower panels present the absolute difference in NTL magnitude between those derived from k-day composite data ( $k \geq 3$ ) and daily observation (1-day composite). The left and right panels show the overall difference and the intra-annual difference (or magnitude), respectively.

difference in NTL magnitude compared with daily observation, from 22% (3d-1d) to 37% (31d-1d) (Fig. 5c). Separately, it increased and decreased the NTL magnitude derived from daily observation by 5 to 9 nWatts/cm<sup>2</sup>/sr and -3 to -8 nWatts/cm<sup>2</sup>/sr, respectively (Fig. 5a). From an intra-annual perspective, the difference was more drastic in summer than in winter, e.g., 39% (summer) vs. 31% (winter) under 31-day composite (Fig. 5d). Taking a further insight, we observed that the difference between daily observation and composite data was much higher than that among composite data. For example, the NTL magnitude difference between daily observation and composite data (30%, 1d vs. mean kd-1d) was about twice as much as the difference among composite data (15%, 3d-1d vs. 31d-1d). Similar results were also found with the modelled NTL magnitude obtained from BFASST model (Fig. S4).

Our results demonstrate that the spatiotemporal pattern of NTL is sensitive to composite period. We ascribe this phenomenon to the enormous variation in daily NTL observations and the number of valid observations within each composite period. Fig. 6a presents the standard deviation of NTL radiance over space and time for each city, as indicators of intra-city spatial and temporal variation, respectively. An extremely high temporal ( $12 \pm 6$  nWatts/cm<sup>2</sup>/sr) and spatial ( $8 \pm 3$  nWatts/cm<sup>2</sup>/sr) variation were observed in daily NTL data. Both variations tapered off as the composite period increased, particularly salient from 1-day to 3-day which decreased by 37% and 8% in temporal and spatial standard deviation, respectively. Such high variation in daily NTL data could be stemmed from the daily variation in illumination patterns and human activities (De Miguel, 2015; Li et al., 2020a; Roman and Stokes, 2015). The uncertainties in VNP46 product and VIIRS instrument also play a non-negligible part, such as the angular effect (Li et al., 2019; Tan et al., 2022), false alarm and leakage of cloud and snow mask (Wang et al., 2020), geometric effect (Wang et al., 2021a), short dwelling time (VIIRS DNB dwell time  $10^{-4}$  s vs. frame rate of the AC lighting  $10^{-2}$  s) (Baker, 2011), and degraded Suomi-NPP VIIRS (increased striping) due to changes in the high gain stage dark offset (Gu et al., 2021). As the composite period becomes longer, the number of valid observations within the composite period increases from 0.4 day (1-day composite) to 15 day (31-day composite) (Fig. 6b). Therefore, when more valid observations are available for generating the composite data, the NTL variation of daily observations can be better reduced and thereby the resulting composite data can be more stable. This also explains the phenomenon that the NTL difference between composite data and daily observation is higher in summer than winter as there are fewer valid observations (Fig. 3) and consequently a higher

NTL variation in summer (9.3 nWatts/cm<sup>2</sup>/sr vs. 7.5 nWatts/cm<sup>2</sup>/sr of winter).

Fig. 7 illustrates the spatial pattern of the NTL magnitude difference between 31-day composite data and daily observation. The difference was significantly larger for cities in more urbanized cities, mostly located in coastal line, such as Shanghai (38%) vs. Xining (12%). At an intra-city angle, similarly, the NTL difference in highly developed regions (e.g., downtown areas) was higher than urban outskirt, which can even exceed 50% in core commercial areas (Fig. 7d). It suggests a close association between the impact of temporal compositing and socioeconomic development. This finding was further supported by the good correlation between GDP and NTL difference ( $R^2 = 0.41$ ; Fig. 7c). Indeed, highly developed cities and regions are expected to have a higher daily variation in the detected NTL magnitude. First, the human activities in these regions encompass more temporal variation and are more unstable than their less-developed counterparts. For example, the illumination from the commercial areas, as a main source of the detected NTL, could be greatly enhanced during the weekends, public events and commercial activities (Roman and Stokes, 2015). Second, as the orbit period of Suomi-NPP is 16-day, different dates of VIIRS data also mean different viewing angles and different local overpass times. The angular effect could be another major cause of a high NTL variation in downtown areas (Tan et al., 2022). Regressing the floor number (a proxy of building height) against the NTL difference of Shanghai ( $R^2 = 0.35$ ; Fig. 7b), it showed that complicated spatial configuration of highly developed areas, especially areas with high-rise vertical structure, would be subject to a stronger angular effect and thus a higher NTL variation. Besides, entangled with angular effect, the varying local overpass time would also increase NTL variation (Wang et al., 2021a).

#### 4.3. Temporal compositing influence on NTL-based applications

##### 4.3.1. Characterizing gradual changes

###### a. Urban mapping based on spectral feature

The mean overall accuracy-period curve summarized from all test cities showed the performance of spectral feature based urban mapping was positively related to composite period (Fig. 8). Compared with daily observation, using composite data increased the urban mapping accuracy by on average 9.7% across periods. The performance improvement can reach up to 34% (e.g., Yanzhou). It was found that using daily observation or data in short composite periods ( $\leq 5$ -day) resulted in

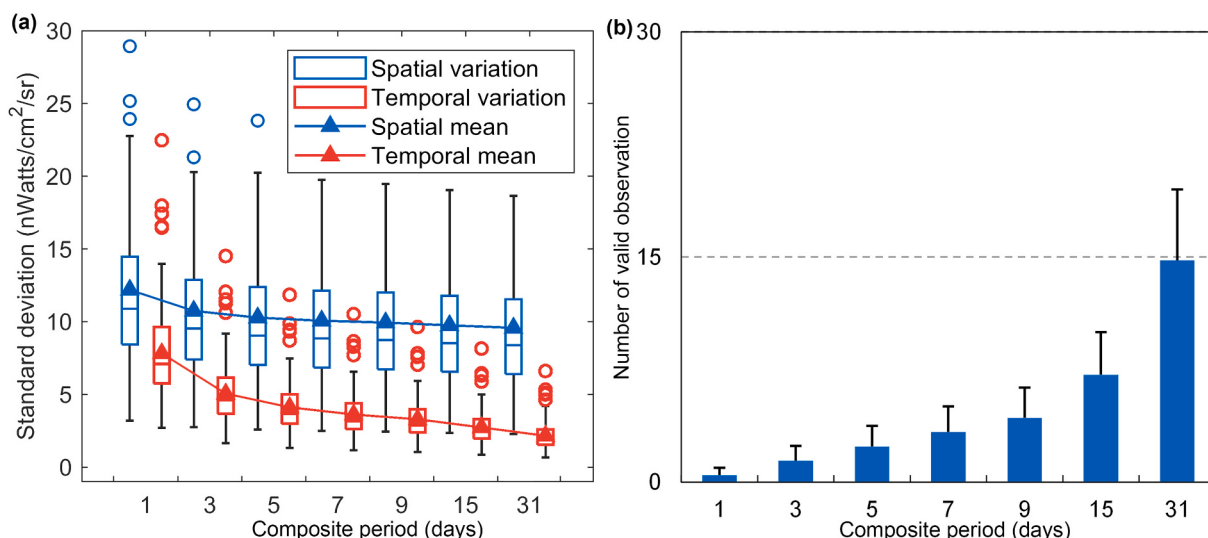


**Fig. 6.** Spatial and temporal variations within each city, reflected by the standard deviation of NTL radiance over space and time, across composite periods (a). Number of valid observations within each composite period (b).

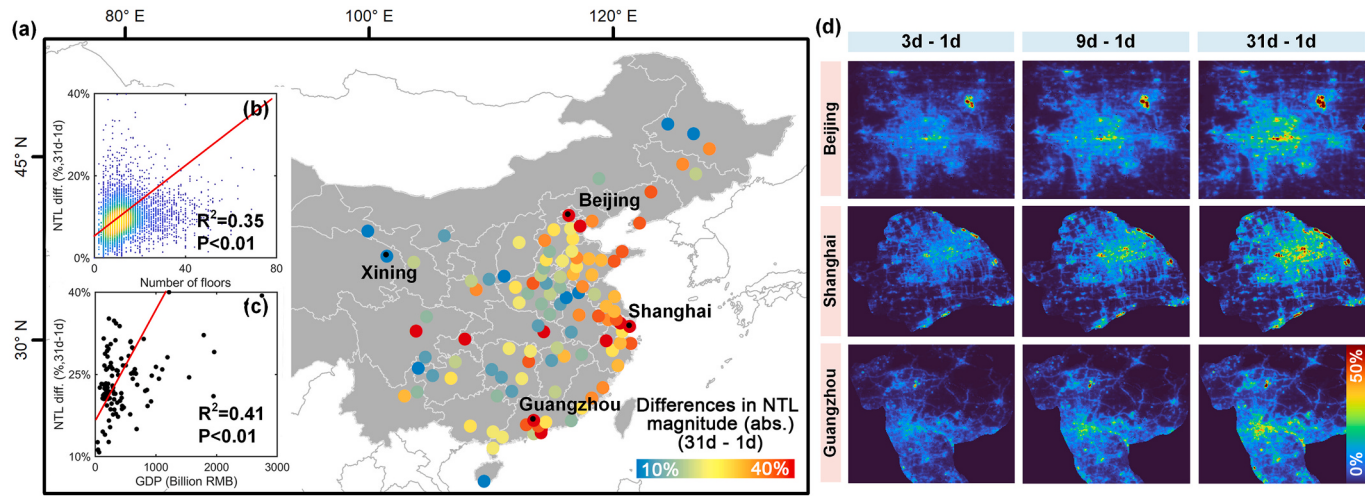


**Fig. 7.** The spatial pattern of the absolute difference in  $NTL_{ts}$  (i.e., modelled NTL magnitude) between 31-day composite data and daily observation (31d-1d; a). Linear regression between NTL difference and number of building floors of Shanghai (pixel-level) (b) and between NTL difference and GDP (city-level) (c). The absolute  $NTL_{ts}$  difference on three cities, including Beijing, Shanghai, and Guangzhou (d). Note that all the values presented are average values aggregated from all pixel time series from 2012 to 2020.

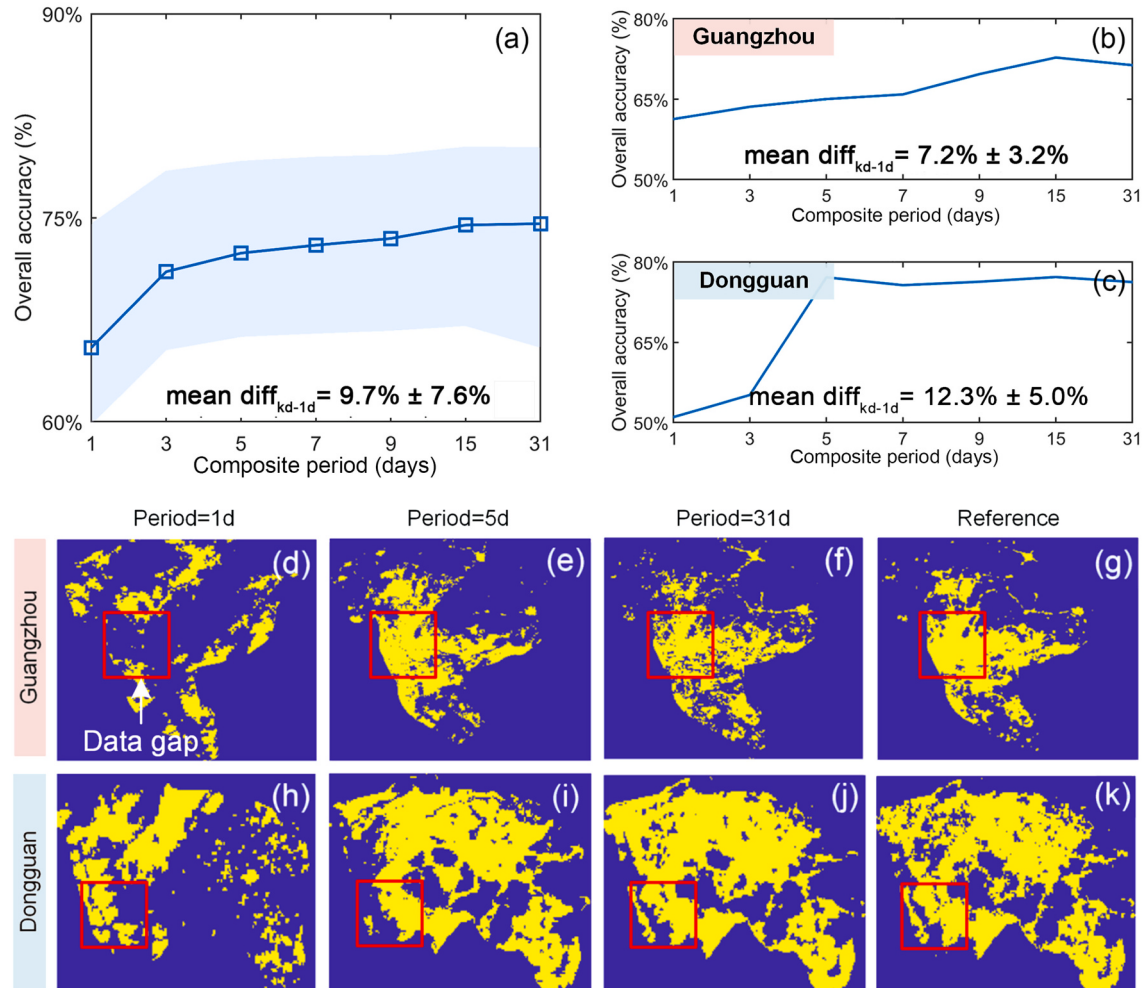


**Fig. 8.** Relationship between composite periods and the accuracy of spectral feature based urban mapping of all cities (a), Guangzhou (b) and Dongguan (c). Comparison of spectral-based urban mapping across periods: Guangzhou (d)-(g) and Dongguan (h)-(k), where 1-d composite are selected from two typical dates partially affected by invalid observations (Guangzhou: DOY201, 2018; Dongguan: DOY039, 2018). The reference urban extent is obtained from MCD12Q1 land cover product.

massive misclassifications and data gaps due to high daily NTL variation and invalid observations (Figs. 8d–8k). However, when longer composite periods were used, these issues were largely improved and the urban mapping performance was maintained at a stable and acceptable level for most cities, such as Guangzhou (Fig. 8b) and Dongguan (Fig. 8c).

#### b. Urban mapping based on temporal and spectral features

In stark contrast, when incorporating temporal features from NTL time series with spectral features, temporal compositing showed insignificant influence on urban mapping accuracy ( $P > 0.01$ ; Fig. S8). Consistent and acceptable urban mapping accuracies were obtained for all test composite periods. This phenomenon was likely because NTL time series in high frequency observations provided a more accurate description of NTL change trajectory, which consequently secured a promising urban mapping accuracy (Zhu, 2017). It also suggests that

NTL data in long composite periods, e.g., bi-monthly or yearly, might impair the mapping accuracy due to an insufficient number of input data and an inaccurate description of the temporal pattern of NTL time series.

Summarizing results from (a) and (b), we found that for traditional urban mapping methods, high frequency urban change mapping with stable and robust performance could be obtained via temporal compositing. More importantly, the great potential of high frequency NTL observations (e.g., VNP46A2) in characterizing long-term graduate changes can be better leveraged by incorporating temporal features.

#### 4.3.2. Detecting abrupt NTL changes

To assess the impact of composite period on abrupt NTL change detection, we quantified the differences in the detected timing of change derived from daily observation and from composite data (Fig. 9). The change detection accuracy was found negatively related to the composite period. The difference in change timing was significantly enlarged

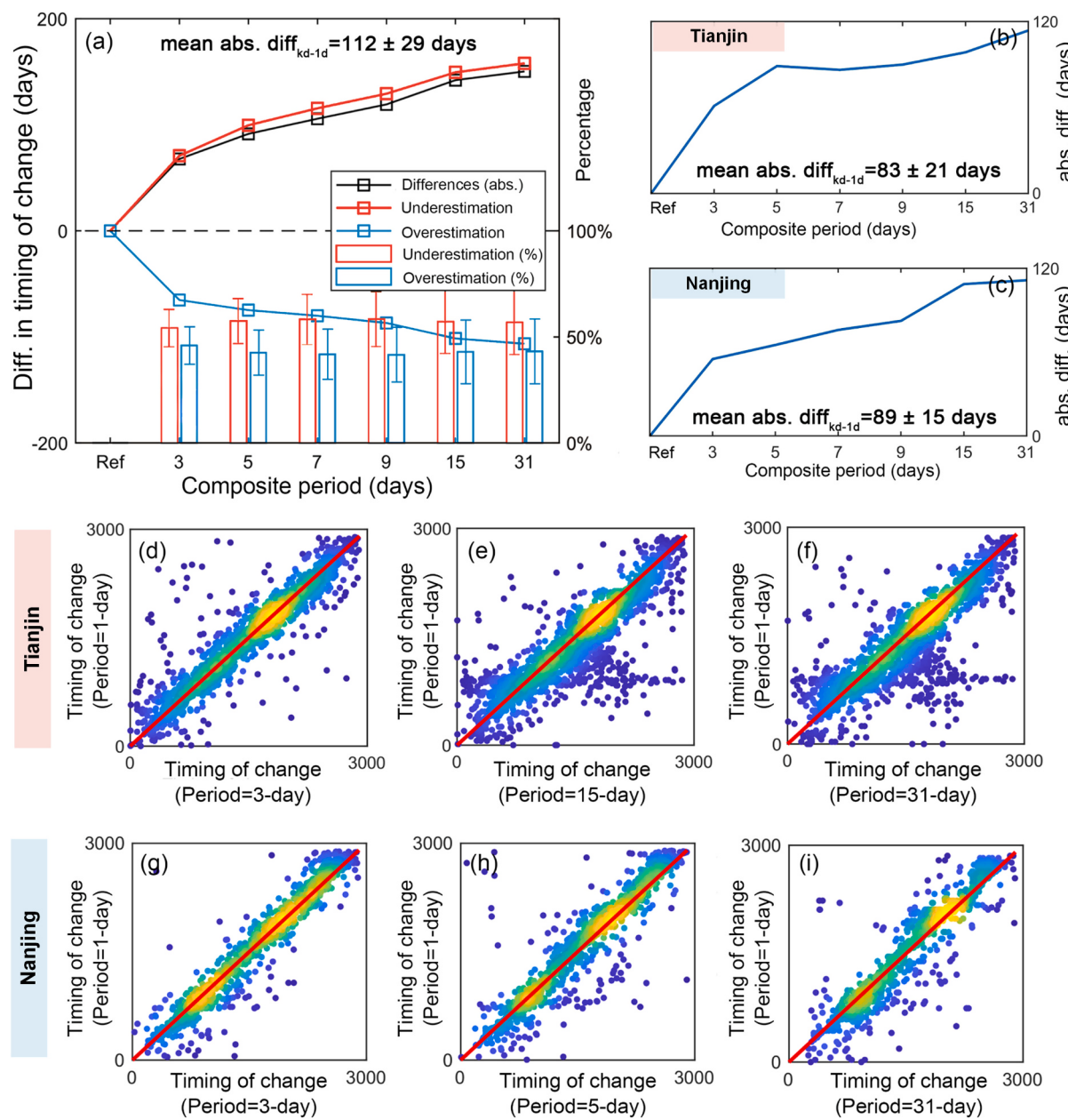


**Fig. 9.** Differences in the timing of detected changes ( $t$ -th day of observation) between composite data and daily observation, for all cities (a), Tianjin (b, d-f) and Nanjing (c, g-i). Underestimation indicates the detected timing of change derived from composite data is later than that from daily observation, while overestimation indicates the detected timing of the change from composite data is earlier than that from daily observation.

along with the increase of composite period, from 67 days with 3-day composite data to 150 days with 31-day composite data. This finding demonstrates the performance of NTL change detection is sensitive to composite period, for which high frequency observations is necessary to ensure accurate detection of abrupt NTL changes.

#### 4.3.3. Monitoring seasonal changes

Fig. 10 demonstrates the impact of temporal compositing on monitoring re-occurring seasonal NTL changes. The modelling  $R^2$  was noticeably improved with a longer composite period. The mean improvement of  $R^2$  comparing k-day composite and daily observation ranged from 0.15–0.57. This finding showed that the seasonality was better captured with composite data (e.g., monthly-composite). On the other hand, it does not necessarily suggest the absence of seasonal changes under short composite periods because the seasonality could merely be overwhelmed by high data variations (Figs. 10d & 10h). As the composite period reached over 5-day, statistically significant ( $P < 0.01$ ) seasonal NTL changes were detected in more than 99% of the pixels in a city (Fig. S9). The analyses comparing the difference in NDVI and NTL between summer and winter, carried out by Román et al. (2018) and our study, both corroborated that the seasonal effect was not negligible in daily VIIRS data (Fig. S12). The mechanism of seasonal effect is inherently complicated because it depends on multiple factors, such as vegetation types (e.g., deciduous forest vs. evergreen forest),

vegetation structure and function, and urban canopy structure. These factors vary over space and time and intertwine with each other, hindering an ideal characterization of the seasonal effect (Levin, 2017; Wang et al., 2021a). Our findings indicate that end-users should be cautious in using high frequency NTL observations in monitoring seasonal changes, as well as interpreting the results.

#### 4.3.4. Impact of temporal compositing across space and types

Figs. 11a-c present the geographic variation of the temporal compositing's influence on NTL-based applications at a city-level basis. Although the impact of temporal composite, represented by the mean  $\text{diff}_{\text{kd-1d}}$  of performance indicators (also see the max  $\text{diff}_{\text{kd-1d}}$  in Fig. S13), were spatially clustered (Global Moran's I  $P < 0.01$ ), the impact varied greatly over space and application types (as demonstrated in Section 4.3.1–4.3.3). Summarizing the CV of three applications, we found the performance of characterizing gradual changes and detecting abrupt changes showed overwhelmingly high variations over space (0.80 and 0.86) than over composite periods (0.09 and 0.20). By comparison, the performance of monitoring seasonal changes was more sensitive over composite periods (0.54) than over space (0.28).

## 5. Conclusions

In this study, using the NASA's Black Marble VIIRS product

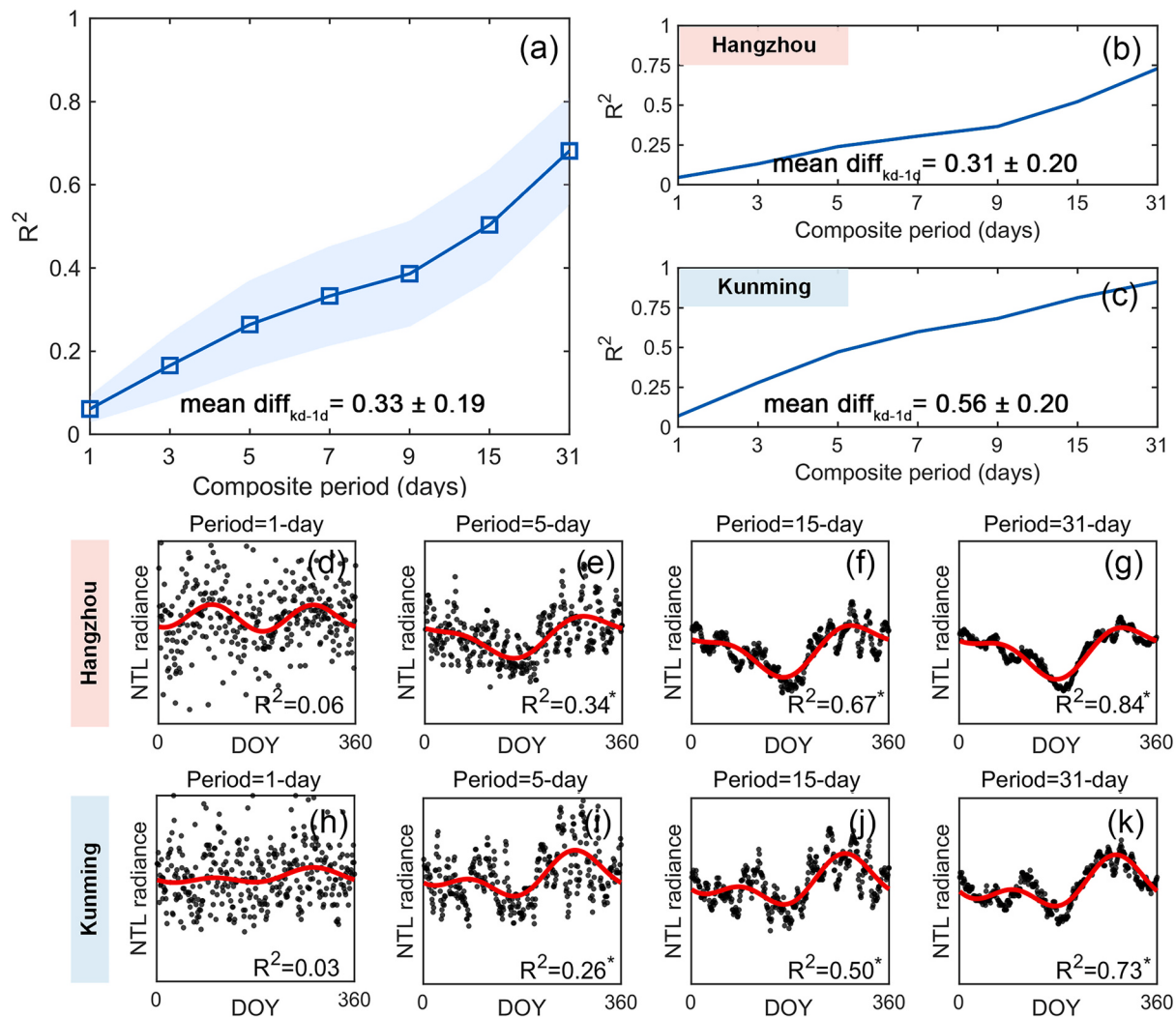


**Fig. 10.**  $R^2$  of seasonality modelling across different composite periods (a). Examples of seasonality modelling across periods: Hangzhou (b, d-g) and Kunming (c, h-k). Two typical urban pixels are selected: 120.085°E/30.260°N (d-g) and 102.725°E/25.038°N (h-k). \* indicates  $P < 0.01$ .

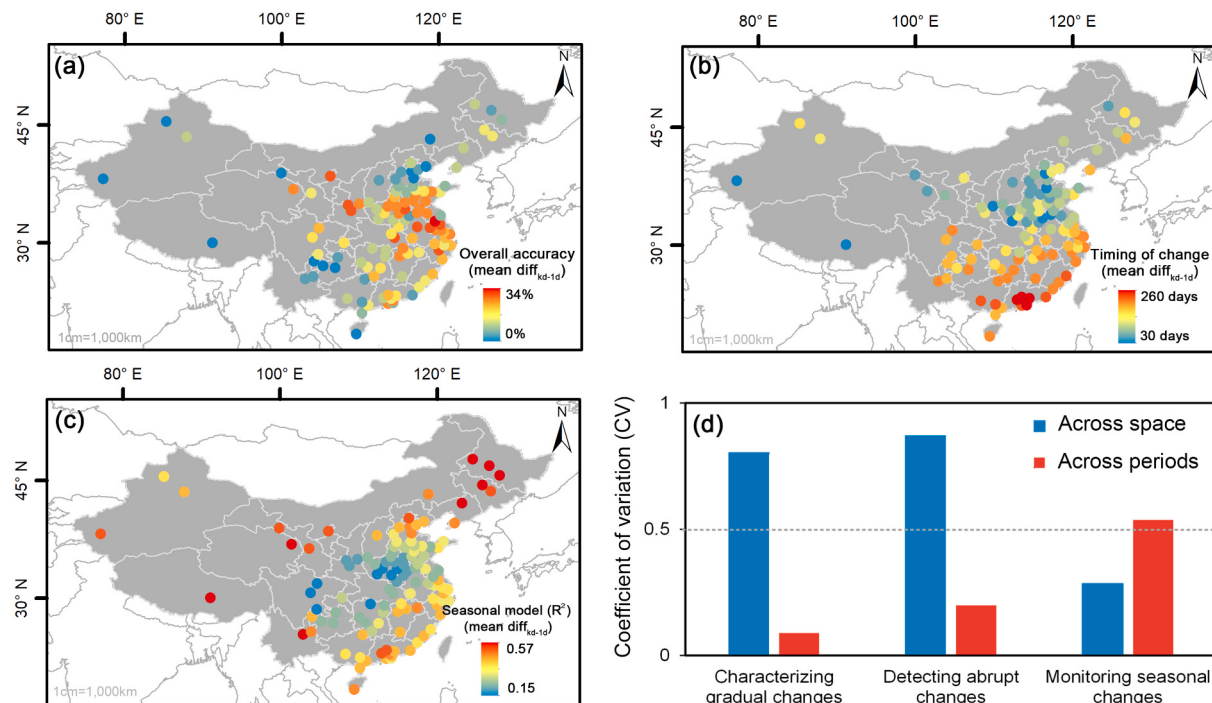


**Fig. 11.** The performance of three NTL-based applications across composite periods: characterizing gradual changes (spectral feature based urban mapping) (a); detecting abrupt changes (b); monitoring seasonal changes (c). Each dot presents the mean difference between results derived from k-day composite and daily observation. The coefficient of variation (CV) of temporal compositing's impact on NTL-based applications across space and composite periods (d).

(VNP46A2), we explored the influence of composite period on valid coverage, spatiotemporal pattern and application of NTL data. Our assessment showed invalid observation was a prevailing issue in daily VIIRS data, while temporal compositing was an imperative and effective way to improve sufficient valid coverage. It required on average a composite period of  $16 \pm 7$  day to safeguard at least 95% valid coverage in a city. The response of valid coverage to the composite period was associated with the climatic setting of a city, including cloud coverage and precipitation condition. Cities in low altitude and pluvial regions required a longer  $\text{Period}_{\text{valid},\text{cvg}}(\alpha)$  than those in dry and continental regions. The spatiotemporal pattern of NTL data was sensitive to composite period. Temporal composite reduced the spatiotemporal variation of NTL data and greatly deviated the NTL magnitude from daily observation by 22–37%, particularly in highly developed cities and regions. The noticeable impact of temporal composite on NTL pattern was attributable to the number of valid observations within the composite period and the high variation of daily NTL observations, which stemmed from the daily variations in human activities and the uncertainties in VNP46 product and VIIRS instrument. Analysis of the relationship between the performance of three typical NTL-based applications and composite period showed that the effect varied greatly across location of the city and application types.

In addition to the current V001 collection of NASA's VNP46 product, there are several daily NTL products available, such as the daily VIIRS product from Earth Observation Group (EOG) at Payne Institute, NOAA-20 satellite, and the upcoming V002 VNP46 product, as well as their corresponding monthly and yearly products, e.g., VNP46A3/A4 (Cao et al., 2021; Elvidge et al., 2021; Wang et al., 2021a). Although studies using daily NTL data are still at their early stage, we expect a boom in using high quality daily NTL and especially its composite data in the near future.

Our study brings tangible benefits to future studies. Revealing the relationship between NTL data and composite period is a timely complement towards a better understanding of uncertainties in NTL data processing and applications. End-users of NTL data could make the best use of the current and upcoming daily VIIRS data by minimizing the

processing loads and uncertainties whilst maximizing the temporal details and application performance. Specifically, we make the following recommendations for future NTL studies. (1) Selecting NTL data in a suitable composite period according to the application: for most applications, it is recommended to use composite data as they can ensure sufficient valid coverage and improve application performance (e.g., urban growth mapping), while for some applications, however, it is a must to use daily observations. For example, short-term/abrupt changes might only be accurately detected with daily observations. (2) Paying attention to the inherent defects of both daily observations and composite data: the users should be cautious about the high data variation and uncertainties of daily observations and the differences in the spatiotemporal pattern presented by daily observations and composite data, as well as varied impacts of these defects on NTL applications.

We conclude by suggesting the following analyses and improvements: First, in this study, only seven composite periods were used, while including more composite periods to examine its influence on NTL data can help to better characterize the relationship between temporal composite period and NTL data. Second, a few factors that can potentially affect the quality of temporal composite NTL data are worthwhile further scrutinies, such as on-orbit calibration performance (Chen et al., 2021), spectral effects (Elvidge et al., 2010) and COVID-19 (Bustamante-Calabria et al., 2021). Third, we based our analysis on the NASA's Black Marble product, instead of other daily VIIRS products. Due to the differences in the processing algorithms in daily VIIRS products, such as atmospheric-, lunar- and stray light corrections, different input NTL products might cause varied responses to temporal composite. Analysis with multi-source daily VIIRS data would be beneficial to further clarification on this issue. At last, our optimal periods for the NTL-based applications could be adopted for a wide variety of NTL applications. However, several NTL processing and applications are falling out of our consideration, such as research involving both DMSP-OLS and VIIRS (X. Li et al., 2020b) and coloration of NTL images (Rybniкова et al., 2021). The impact of compositing on these processing and applications should be explored.

## CRediT authorship contribution statement

**Qiming Zheng:** Conceptualization, Methodology, Software, Formal analysis, Writing – original draft, Writing – review & editing, Funding acquisition. **Qihao Weng:** Conceptualization, Writing – review & editing. **Yuyu Zhou:** Conceptualization, Writing – review & editing. **Baiyu Dong:** Resources, Data curation, Writing – review & editing.

## Declaration of Competing Interest

The authors declare that they have no known competing financial interests or personal relationships that could have appeared to influence the work reported in this paper.

## Acknowledgement

We thank our student intern Ms. Nicole Chung Mae Sze for her assistance in data collection. This research is supported by the National Research Foundation, Singapore, under its NRF Returning Singaporean Scientists Scheme (NRF-RSS2019-007) and the College of Liberal Arts and Sciences Dean's Emerging Faculty Leaders Award at Iowa State University.

## Appendix A. Supplementary data

Supplementary data to this article can be found online at <https://doi.org/10.1016/j.rse.2022.113016>. Codes to process and analyze the NASA's Black Marble VIIRS images can be found online at: <https://github.com/qmzheng09work>.

## References

- Anderson, S.J., Tuttle, B.T., Powell, R.L., Sutton, P.C., 2010. Characterizing relationships between population density and nighttime imagery for Denver, Colorado: issues of scale and representation. *Int. J. Remote Sens.* 31 (21), 5733–5746. <https://doi.org/10.1080/01431161.2010.496798>.
- Baker, N., 2011. Joint polar satellite system (JPSS) VIIRS geolocation algorithm theoretical basis document (ATBD), 474 (00053), 144.
- Bustamante-Calabria, M., Sánchez de Miguel, A., Martín-Ruiz, S., Ortiz, J.-L., Vilchez, J.M., Pelegrina, A., Gaston, K.J., 2021. Effects of the COVID-19 lockdown on urban light emissions: ground and satellite comparison. *Remote Sens.* 13 (2) <https://doi.org/10.3390/rs13020258>.
- Cao, C., Zhang, B., Shao, X., Wang, W., Upadhyay, S., Choi, T., Kalluri, S., 2021. Mission-long recalibrated science quality suomi NPP VIIRS radiometric dataset using advanced algorithms for time series studies. *Remote Sens.* 13 (6) <https://doi.org/10.3390/rs13061075>.
- Chen, X., 2020. Nighttime lights and population migration: revisiting classic demographic perspectives with an analysis of recent European data. *Remote Sens.* 12 (1), 169.
- Chen, H., Sun, C., Xiong, X., Sarid, G., Sun, J.J.R.S., 2021. SNPP VIIRS day night band: ten years of on-orbit calibration and performance. *Remote Sens.* 13 (20), 4179.
- Croft, T.A., 1978. Nighttime images of the earth from space. *Sci. Am.* 239 (1), 86–101.
- De Miguel, A.S., 2015. Spatial, Temporal and Spectral Variation of Light pollution and its sources: Methodology and Resources. Doctoral dissertation. Institute of Astrophysics of Andalusia, Madrid, Spain.
- Didan, K., 2015. MOD13A1 MODIS/Terra Vegetation Indices 16-Day L3 Global 500 m SIN Grid V006 (NASA EOSDIS Land Processes DAAC, accessed 24 Aug 2020), 10.5067/MODIS. In: MOD13A1.
- Elvidge, C., Baugh, K., Kihn, E.A., Kroehl, H.W., Davis, E.R., 1997. Mapping city lights with nighttime data from the DMSP operational linescan system. *Photogramm. Eng. Remote. Sens.* 63 (6), 727–734. Retrieved from [://WOS:A1997XC40700009](https://doi.org/10.3390/s100403961).
- Elvidge, C.D., Keith, D.M., Tuttle, B.T., Baugh, K.E., 2010. Spectral identification of lighting type and character. *Sensors (Basel)* 10 (4), 3961–3988. <https://doi.org/10.3390/s100403961>.
- Elvidge, C., Baugh, K., Zhizhin, M., Hsu, F.C., Ghosh, T., 2017. VIIRS night-time lights. *Int. J. Remote Sens.* 38 (21), 5860–5879. <https://doi.org/10.1080/01431161.2017.1342050>.
- Elvidge, C.D., Hsu, F.-C., Zhizhin, M., Ghosh, T., Taneja, J., Bazilian, M., 2020. Indicators of electric power instability from satellite observed nighttime lights. *Remote Sens.* 12 (19) <https://doi.org/10.3390/rs12193194>.
- Elvidge, C.D., Zhizhin, M., Ghosh, T., Hsu, F.-C., Taneja, J., 2021. Annual time series of global VIIRS nighttime lights derived from monthly averages: 2012 to 2019. *Remote Sens.* 13 (5) <https://doi.org/10.3390/rs13050922>.
- Gemmer, M., Becker, S., Jiang, T., 2004. Observed monthly precipitation trends in China 1951–2002. *Theor. Appl. Climatol.* 77 (1), 39–45.
- Gorelick, N., Hancher, M., Dixon, M., Ilyushchenko, S., Thau, D., Moore, R., 2017. Google Earth Engine: planetary-scale geospatial analysis for everyone. *Remote Sens. Environ.* 202, 18–27. <https://doi.org/10.1016/j.rse.2017.06.031>.
- Gu, Y., Blonski, S., Shao, X., Upadhyay, S., Cao, C., 2021. Restoration of degraded Suomi-NPP VIIRS DNB nighttime imagery induced by electronic bias change. In: Paper presented at the Earth Observing Systems XXVI.
- Guk, E., Levin, N., 2020. Analyzing spatial variability in night-time lights using a high spatial resolution color Jilin-1 image–Jerusalem as a case study. *ISPRS J. Photogramm. Remote Sens.* 163, 121–136.
- Henderson, M., Yeh, E.T., Gong, P., Elvidge, C., Baugh, K., 2003. Validation of urban boundaries derived from global night-time satellite imagery. *Int. J. Remote Sens.* 24 (3), 595–609.
- Hong, Y., Wu, B., Song, Z., Li, Y., Wu, Q., Chen, Z., Yu, B., 2021. A monthly night-time light composite dataset of NOAA-20 in China: a multi-scale comparison with S-NPP. *Int. J. Remote Sens.* 42 (20), 7931–7951. <https://doi.org/10.1080/01431161.2021.1969057>.
- Hu, L., Brunsell, N.A., 2013. The impact of temporal aggregation of land surface temperature data for surface urban heat island (SUHI) monitoring. *Remote Sens. Environ.* 134, 162–174. <https://doi.org/10.1016/j.rse.2013.02.022>.
- Huffman, G.J., Bolvin, D.T., Braithwaite, D., Hsu, K., Joyce, R., Xie, P., Yoo, S.J., 2015. NASA global precipitation measurement (GPM) integrated multi-satellite retrievals for GPM (IMERG), 4, p. 26.
- Hüttich, C., Herold, M., Wegmann, M., Cord, A., Strohbach, B., Schmullius, C., Dech, S., 2011. Assessing effects of temporal compositing and varying observation periods for large-area land-cover mapping in semi-arid ecosystems: Implications for global monitoring. *Remote Sens. Environ.* 115 (10), 2445–2459. <https://doi.org/10.1016/j.rse.2011.05.005>.
- Imhoff, M.L., Lawrence, W.T., Stutzer, D.C., Elvidge, C.D., 1997. A technique for using composite DMSP/OLS "city lights" satellite data to map urban area. *Remote Sens. Environ.* 61 (3), 361–370. Retrieved from [://WOS:A1997XN25300003](https://doi.org/10.1016/S0034-425X(97)89003-3).
- Levin, N., 2017. The impact of seasonal changes on observed nighttime brightness from 2014 to 2015 monthly VIIRS DNB composites. *Remote Sens. Environ.* 193, 150–164. <https://doi.org/10.1016/j.rse.2017.03.003>.
- Levin, N., Kyba, C.C.M., Zhang, Q., de Miguel, A.S., Roman, M.O., Li, X., Elvidge, C.D., 2020. Remote sensing of night lights: a review and an outlook for the future. *Remote Sens. Environ.* 237 <https://doi.org/10.1016/j.rse.2019.111443>.
- Li, X., Zhao, L., Li, D., Xu, H., 2018. Mapping urban extent using Luojia 1–01 nighttime light imagery. *Sensors* 18 (11). <https://doi.org/10.3390/s18113665>.
- Li, X., Ma, R., Zhang, Q., Li, D., Liu, S., He, T., Zhao, L., 2019. Anisotropic characteristic of artificial light at night – Systematic investigation with VIIRS DNB multi-temporal observations. *Remote Sens. Environ.* 233 <https://doi.org/10.1016/j.rse.2019.111357>.
- Li, X., Levin, N., Xie, J., Li, D., 2020a. Monitoring hourly night-time light by an unmanned aerial vehicle and its implications to satellite remote sensing. *Remote Sens. Environ.* 247 <https://doi.org/10.1016/j.rse.2020.111942>.
- Li, X., Zhou, Y., Zhao, M., Zhao, X., 2020b. A harmonized global nighttime light dataset 1992–2018. *Sci. Data* 7 (1), 168. <https://doi.org/10.1038/s41597-020-0510-y>.
- Liu, Z., He, C., Zhang, Q., Huang, Q., Yang, Y., 2012. Extracting the dynamics of urban expansion in China using DMSP-OLS nighttime light data from 1992 to 2008. *Landscape Urban Plan.* 106 (1), 62–72. <https://doi.org/10.1016/j.landurbplan.2012.02.013>.
- Miller, S.D., Turner, R.E., 2009. A dynamic lunar spectral irradiance data set for NPOESS/VIIRS day/night band nighttime environmental applications. *IEEE Trans. Geosci. Remote Sens.* 47 (7), 2316–2329. <https://doi.org/10.1109/tgrs.2009.2012696>.
- NASA, 2018. VNPP46A2 - VIIRS/NPP Gap-Filled Lunar BRDF-Adjusted Nighttime Lights Daily L3 Global 500 m Linear Lat Lon Grid. Retrieved from <https://landsweb.modaps.eosdis.nasa.gov/missions-and-measurements/products/VNP46A2/>.
- Reba, M., Seto, K.C., 2020. A systematic review and assessment of algorithms to detect, characterize, and monitor urban land change. *Remote Sens. Environ.* 242 <https://doi.org/10.1016/j.rse.2020.111739>.
- Roman, M.O., Stokes, E.C., 2015. Holidays in lights: tracking cultural patterns in demand for energy services. *Earth's Future* 3 (6), 182–205. <https://doi.org/10.1002/2014EF000285>.
- Román, M.O., Wang, Z., Sun, Q., Kalb, V., Miller, S.D., Molthan, A., Masuoka, E.J., 2018. NASA's Black Marble nighttime lights product suite. *Remote Sens. Environ.* 210, 113–143. <https://doi.org/10.1016/j.rse.2018.03.017>.
- Román, M.O., Stokes, E.C., Shrestha, R., Wang, Z., Schultz, L., Carlo, E.A.S., Kalb, V., 2019. Satellite-based assessment of electricity restoration efforts in Puerto Rico after Hurricane Maria. *PLoS One* 14 (6), e0218883. <https://doi.org/10.1371/journal.pone.0218883>.
- Rybinkova, N., Portnov, B.A., Mirkes, E.M., Zinov'yev, A., Brook, A., Gorban, A.N., 2021. Coloring panchromatic nighttime satellite images: comparing the performance of several machine learning methods. *IEEE Trans. Geosci. Remote Sens.* 1–15 <https://doi.org/10.1109/tgrs.2021.3076011>.
- Sánchez de Miguel, A., Kyba, C.C.M., Aubé, M., Zamorano, J., Cardiel, N., Tapia, C., Gaston, K.J., 2019. Colour remote sensing of the impact of artificial light at night (I): the potential of the International Space Station and other DSLR-based platforms. *Remote Sens. Environ.* 224, 92–103. <https://doi.org/10.1016/j.rse.2019.01.035>.
- Sánchez de Miguel, A., Zamorano, J., Aubé, M., Bennie, J., Gallego, J., Ocaña, F., Gaston, K.J., 2021. Colour remote sensing of the impact of artificial light at night (II): Calibration of DSLR-based images from the International Space Station. *Remote Sens. Environ.* 264 <https://doi.org/10.1016/j.rse.2021.112611>.

- Sanders, D., Frago, E., Kehoe, R., Patterson, C., Gaston, K.J., 2020. A meta-analysis of biological impacts of artificial light at night. *Nat. Ecol. Evol.* <https://doi.org/10.1038/s41559-020-01322-x>.
- Small, C., Sousa, D., 2021. Spatiotemporal evolution of COVID-19 infection and detection within night light networks: comparative analysis of USA and China. *Appl. Netw. Sci.* 6 (1), 10. <https://doi.org/10.1007/s41109-020-00345-4>.
- Sulla-Menashe, D., Gray, J.M., Abercrombie, S.P., Friedl, M.A., 2019. Hierarchical mapping of annual global land cover 2001 to present: the MODIS collection 6 Land cover product. *Remote Sens. Environ.* 222, 183–194. <https://doi.org/10.1016/j.rse.2018.12.013>.
- Sutton, P.C., 2003. A scale-adjusted measure of “Urban sprawl” using nighttime satellite imagery. *Remote Sens. Environ.* 86 (3), 353–369. [https://doi.org/10.1016/s0034-4257\(03\)00078-6](https://doi.org/10.1016/s0034-4257(03)00078-6).
- Tan, X., Zhu, X., Chen, J., Chen, R., 2022. Modeling the direction and magnitude of angular effects in nighttime light remote sensing. *Remote Sens. Environ.* 269 <https://doi.org/10.1016/j.rse.2021.112834>.
- Tang, Y., Shao, Z., Huang, X., Cai, B., 2021. Mapping impervious surface areas using time-series nighttime light and MODIS imagery. *Remote Sens.* 13 (10), 1900.
- Verbesselt, J., Hyndman, R., Zeileis, A., Culvenor, D., 2010. Phenological change detection while accounting for abrupt and gradual trends in satellite image time series. *Remote Sens. Environ.* 114 (12), 2970–2980. <https://doi.org/10.1016/j.rse.2010.08.003>.
- Wang, Z., Roman, M., Kalb, V., Shrestha, R., Stokes, E., Paynter, I., 2020. Uncertainties in VIIRS nighttime light time series analysis. In: Paper presented at the IGARSS 2020–2020 IEEE International Geoscience and Remote Sensing Symposium.
- Wang, Z., Román, M.O., Kalb, V.L., Miller, S.D., Zhang, J., Shrestha, R.M., 2021a. Quantifying uncertainties in nighttime light retrievals from Suomi-NPP and NOAA-20 VIIRS Day/Night Band data. *Remote Sens. Environ.* 263 (112), 557. <https://doi.org/10.1016/j.rse.2021.112557>.
- Wang, Z., Shrestha, R., Román, M.O., 2021b. NASA’s black marble nighttime lights product suite algorithm theoretical basis document (ATBD). Version 1, 2. Retrieved from <https://blackmarble.gsfc.nasa.gov/>.
- Xiao, P., Wang, X., Feng, X., Zhang, X., Yang, Y., 2014. Detecting China’s urban expansion over the past three decades using nighttime light data. *IEEE J. Select. Top. Appl. Earth Observ. Remote Sens.* 7 (10), 4095–4106. <https://doi.org/10.1109/jstars.2014.2302855>.
- Xie, Y., Weng, Q., Fu, P., 2019. Temporal variations of artificial nighttime lights and their implications for urbanization in the conterminous United States, 2013–2017. *Remote Sens. Environ.* 225, 160–174. <https://doi.org/10.1016/j.rse.2019.03.008>.
- Zhao, X., Yu, B., Liu, Y., Yao, S., Lian, T., Chen, L., Wu, J., 2018. NPP-VIIRS DNB daily data in natural disaster assessment: evidence from selected case studies. *Remote Sens.* 10 (10) <https://doi.org/10.3390/rs10101526>.
- Zhao, N., Liu, Y., Hsu, F.-C., Samson, E.L., Letu, H., Liang, D., Cao, G., 2020. Time series analysis of VIIRS-DNB nighttime lights imagery for change detection in urban areas: a case study of devastation in Puerto Rico from hurricanes Irma and Maria. *Appl. Geogr.* 120 <https://doi.org/10.1016/j.apgeog.2020.102222>.
- Zheng, Q., Weng, Q., Huang, L., Wang, K., Deng, J., Jiang, R., Gan, M., 2018. A new source of multi-spectral high spatial resolution night-time light imagery—JL1-3B. *Remote Sens. Environ.* 215, 300–312. <https://doi.org/10.1016/j.rse.2018.06.016>.
- Zheng, Q., Weng, Q., Wang, K., 2019. Developing a new cross-sensor calibration model for DMSP-OLS and Suomi-NPP VIIRS night-light imageries. *ISPRS J. Photogramm. Remote Sens.* 153, 36–47. <https://doi.org/10.1016/j.isprsjprs.2019.04.019>.
- Zheng, Q., Weng, Q., Wang, K., 2021. Characterizing urban land changes of 30 global megacities using nighttime light time series stacks. *ISPRS J. Photogramm. Remote Sens.* 173, 10–23. <https://doi.org/10.1016/j.isprsjprs.2021.01.002>.
- Zhou, Y., Smith, S.J., Elvidge, C.D., Zhao, K., Thomson, A., Imhoff, M., 2014. A cluster-based method to map urban area from DMSP/OLS nightlights. *Remote Sens. Environ.* 147, 173–185. <https://doi.org/10.1016/j.rse.2014.03.004>.
- Zhou, Y., Li, X., Asrar, G.R., Smith, S.J., Imhoff, M., 2018. A global record of annual urban dynamics (1992–2013) from nighttime lights. *Remote Sens. Environ.* 219, 206–220. <https://doi.org/10.1016/j.rse.2018.10.015>.
- Zhu, Z., 2017. Change detection using landsat time series: A review of frequencies, preprocessing, algorithms, and applications. *ISPRS J. Photogramm. Remote Sens.* 130, 370–384. <https://doi.org/10.1016/j.isprsjprs.2017.06.013>.
- Zhu, Z., Zhou, Y., Seto, K.C., Stokes, E.C., Deng, C., Pickett, S.T.A., Taubenböck, H., 2019. Understanding an urbanizing planet: strategic directions for remote sensing. *Remote Sens. Environ.* 228, 164–182. <https://doi.org/10.1016/j.rse.2019.04.020>.